

Periodicity Irregularity Map Estimation of Human Gait with a Depth Camera for Pathology Detection

Didier Ndayikengurukiye, Max Mignotte

DIRO (Département d'Informatique et de Recherche Opérationnelle)
Université de Montréal, Faculté des Arts et des Sciences, Montréal, H3C 3J7, QC, Canada

NDAYIKED@IRO.UMONTREAL.CA
MIGNOTTE@IRO.UMONTREAL.CA

Abstract—This paper describes a computer vision system based on a depth camera (Microsoft Kinect™) and a conventional treadmill for a fast and reliable visual detection and analysis of the patient's body parts that have an irregular movement pattern, in terms of periodicity, during walking. In this work, we thus assume that the gait of a healthy subject exhibits anywhere in the human body, during the walking cycles, a depth signal (depending on time and collected by a Kinect™ sensor) with a periodic pattern without noise. Herein, the presence of noise and its importance can be used either as a good indicator of possible pathology in an early (and fast) diagnostic tool or to provide information about the presence and extent of disease or (orthopedic, muscular or neurological) problems in the patient. The depth videos used show, for each one, the gait cycles of either a healthy individual or simulating an orthopedic problem (with the presence of a heel under the right or left foot). The proposed system is able to estimate, from each video sequence, a saliency color map showing the areas of strong gait irregularities, in terms of periodicity (also called aperiodic noise energy), of each subject. Even if the maps obtained are informative and highly discriminant for a direct visual classification, even for a non-specialist, the proposed system, based on the extraction/classification of features from each obtained map allow us to automatically detect maps representing healthy individuals and those representing individuals with orthopedic problems.

Index Terms—Gait analysis, Gait classification, Aperiodic noise, Irregular periodicity, Pathology detection, Kinect depth sensor

I. INTRODUCTION

THE interest in human motion already existed in classical antiquity and depending on needs and tools available, its

The authors are with the vision lab. of the Département d'Informatique et de Recherche Opérationnelle (DIRO), Université de Montréal, Faculté des Arts et des Sciences, Montréal, H3C 3J7, QC, Canada, E-mails: {ndayiked, mignotte}@iro.umontreal.ca

study has been progressing over the years [1]. As stated by Rose and Gamble [2], even if human walking is seemingly simple, it remains a complex activity (involving balance, timing and coordination of sight and the other senses) whose complexity is revealed if we try to make its qualitative or quantitative description. Every person walking has characteristics of its own (while also sharing several common characteristics of human gait). This is such a familiar experience that in our life we have recognized, at least one day, a person by his walk. This may explain why some researchers study human gait in perspective of human identification [3]–[5] using different techniques and materials for extracting the features used in classification. For example, Gafurov et al. used accelerometer as material [6], Verlekar et al. [7] et Iwashita et al. [8] used shadow information to characterize gait, Dupuis et al. [9] applied feature subset selection, to name but a few. However, the study of human gait has many other areas of application: robotics (e.g., studies on passive dynamic walking), sport sciences [10] (e.g., modeling of athlete motion) [1], video surveillance applications, advanced human computer interfaces or medicine (e.g., rehabilitation technology) etc. Bauckhage et al. [11] noticed that not only human gait analysis allows the person identification and activity recognition, but it can also help in detecting abnormalities in people's health. Thus, human gait has applications related to diseases that prevent patients from walking normally [12], [13]. The abnormalities generated by diseases and which may alter the *natural* (bio)mechanics of walking can be classified into five categories: deformity, muscle weakness, sensory loss, pain, and impaired motor control [14].

Most accurate systems, for data acquisition in the study of human movement, are systems with markers [15], [16] but the need for systems without markers also arises [17]. Indeed,

these marker-based systems are able to give very accurate but also sparse (and generally not distributed equidistantly) measures over the body. In addition, the high cost of these high-end systems [18] inhibit their widespread usage for routine clinical practices.

In this work, we will focus on how to design and implement a new gait analysis system, from a depth camera placed in front of a subject walking on a conventional treadmill, capable of detecting these above-mentioned abnormalities and to quantify their severity and also to localize the different damaged or impaired body parts of the patient. We are also interested in developing a low cost, without markers, non-invasive and simple to set-up, easy to use and fast computer vision based system while being accurate and reliable, for a rapid clinical diagnosis used as a first interesting screening for a possible (orthopedic, muscular or neurological) disease, prior to a more thorough examination by a specialist doctor.

II. PREVIOUS WORK

Most research works on gait analysis (for possible clinical applications) use systems with markers and multiple cameras [19]–[21]. But other systems, less invasive and less difficult to handle, such as insoles [20], [22], wireless shoes [23], accelerometers [24]–[26] and Microsoft KinectTM depth cameras [27] are now also increasingly being used.

In this latter case, Kinect can provide a depth image which is useful for the development of in-home monitoring systems that automatically detect when falls have occurred or when the risk of falling is increasing [28], [29] or directly provide the skeleton [30] data information for the automated estimation of children's (spatial and temporal) gait parameters [31] or to extract an accurate and reliable set of gait features [32], thanks to a regression approach (based on an ensemble of regression trees). More generally, the full body skeleton information provided by Kinect can also be efficiently used for human gait [33] or posture recognition [34] or body tracking in the context of health applications (coaching or physical exercise of the elderly population) [35], to name a few [36].

As proposed herein, the research works introduced in [37] and in [38] also use, for data acquisition, a treadmill and a Microsoft KinectTM depth camera. These studies support the hypothesis that a symmetrical gait is generally expected in the case of healthy people. For example, in [37] a depth energy image (DEI) which is, in fact, the pixel-wise mean of all images in the input depth image sequence (over a gait cycle, or a longer period), is first estimated. Then, an abnormal gait is detected from a normal one because a symmetric healthy walk use to generate a DEI exhibiting a symmetric silhouette,

in terms of mean depth (energy) and conversely. This two-class detection is then achieved through the measurement of asymmetry indexes, from the DEI. Although, this feasibility study gives good results, it was only tested on 6 subjects. Using the same important concept of gait symmetry in healthy subjects, walking abnormalities are also detected in [38]. In this work, a spatial and temporal registration procedure allows to divide each gait cycle in two sub-cycles (left and right steps) and the comparison between these two sub-cycles, at lower limbs, in term of depth difference, allows to efficiently detect an abnormal gait from a normal one and to also quantify the degree of asymmetry of the lower body. Let us also mention the system proposed in [39], which is not used for classification (between healthy or unhealthy gait) but that allows to estimate an interesting color map providing a quick overview (in terms of perceptual color difference) of asymmetries existing in the gait cycle of a subject.

In the same spirit, but with a single triaxial accelerometer (providing simultaneous measurements in three orthogonal directions), Moe-Nilssen and Helbostad [40] have estimated human gait parameters like cadence, step length, and measures of gait regularity and symmetry from subjects at free walking speeds.

Contrary to the aforementioned works, our model is not based on asymmetry detection (between left and right lower limbs) as an indicator of possible pathology but rather on the amount of noise altering an *ideal* periodic depth movement of each part of the human body during walking. In our model, we thus assume that the gait of a healthy subject exhibits, anywhere in the human body, during the walking cycles, a depth signal (depending on time and collected a KinectTM sensor) with a periodic pattern without noise. The proposed system is able to estimate, from each video sequence, a color map visualizing the areas of strong gait irregularities, in terms of periodicity, on the patient's body silhouette. In order to get a reliable estimation of this aperiodic noise energy map we have decided to estimate it, in two fully complementary ways, namely in the temporal and in the frequency domains. This strategy allows us to get two different estimations leading to different estimation errors which can then be efficiently combine in order to improve the classification result in a (complementary) fusion way, in terms of information interaction [41]. This map is clearly informative and highly discriminant for a direct visual classification, even for a non-specialist. Herein, the location and degree of noise (representing the degree of gait irregularities) can be used as a good indicator of possible pathology or to provide information about the presence and extent of medical problems. An automatic system, based on the extraction/classification of features from each obtained

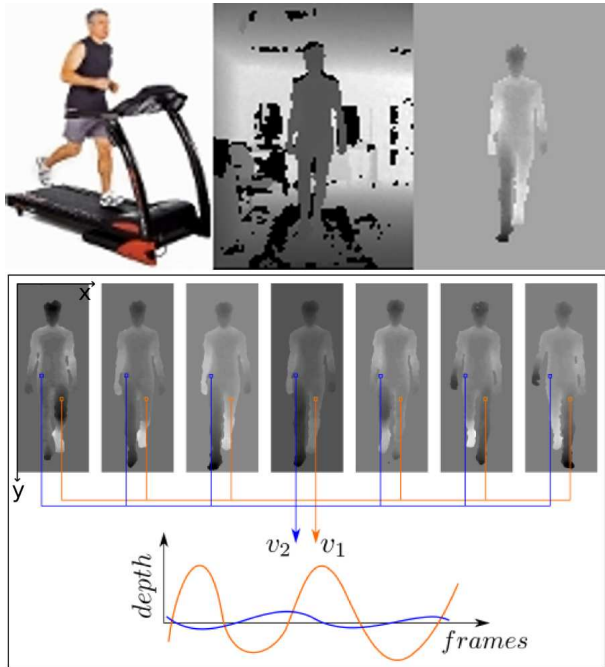


Fig. 1. From lexicographic order; setup and pre-processing steps with respectively the subject walking on a conventional treadmill (Life Fitness F3), the original depth view recorded from Kinect™ and the segmented image (after background and treadmill removal). Example of two depth signals (exhibiting a periodic pattern) for a gait cycle of a human subject.

map is also proposed and allow us to automatically detect maps representing healthy individuals and those representing individuals with orthopedic problems.

III. PROPOSED MODEL

The human gait movement is a remarkable example of collaborative interactions between the articular, musculoskeletal and neurological systems working perfectly (and synchronically) together. When everything is working correctly, the healthy loco-motor system produces a smooth, energy efficient, stable gait, exhibiting, at any point of the body, during walking cycles, a (nice) periodic walking pattern without noise. That is why, gait irregularities in terms of periodicity may be a good indicator (and sometimes the first clinical manifestation) of various health problems. In our application, the degree of gait irregularities in terms of periodicity will be also referred, in the following, as being the concept of degree of aperiodicity and quantified by the aperiodic noise energy

since this concept is very close to the one existing and used in speech processing¹.

For this purpose, our system first propose to estimate a saliency color map, providing both an overview of aperiodic noise energy or irregularity energy, in terms of periodicity, existing in the gait cycle of a patient and also capable of showing the areas of strongest gait irregularities. In our application, this map is estimated from the sequence of depth images captured by a Microsoft Kinect™-style (depth) sensor placed in front of the patient walking on a conventional treadmill. After a habituation period of about 2 minutes, the walking speed of each subject appeared to become constant and their gait movement is then collected by the Kinect™.

The Kinect sensor outputs 30 depth maps per second (30 frames per second), with a resolution of 640 per 480 pixels. Each pixel of the depth image cube (or video sequence) is also a 1D depth signal, evolving through time which, in fact, exhibits a periodic walking pattern, without noise, (see Fig. 1) for a stable, energy efficient, healthy gait.

Each video sequence (of approximately 5 minutes) shows the gait cycles of a healthy person or the one simulating an orthopedic or muscle disease (presence of a troublesome heel under the right or left foot). More precisely, for the experiments, 17 (healthy) subjects (young male adults, 26.7 ± 3.8 years old, 179.1 ± 11.5 cm height and 75.5 ± 13.6 kg with no reported gait issues) were asked to walk normally on a treadmill (Life Fitness F3) with or without simulated length leg discrepancy (LLD). Every patient had to walk normally (group A), then with a 5 cm sole, impairing the normal walk, under the left foot (group B), then with the sole under the right foot (group C), for a total of $17 \times 3 = 51$ video sequences to be classified. The scene took place in a non-cluttered room where the treadmill is always in the same position relatively to the Kinect™ camera. In this way, a silhouette extraction strategy (background and treadmill removal) can be easily defined as proposed in [39].

To this end, in order to get a reliable estimation of this 2D spatial map of irregularities in periodicity, we have decided to estimate it in two different ways. The first one is fully (and only) estimated in the temporal domain whereas the second estimation of this map is only performed in the frequency domain. This strategy allows us to get two different

¹In speech or acoustic signal processing, aperiodic noise is produced by high-frequency (acoustic) energy which is distributed fairly randomly across the upper part of the spectrum. It is distinct from periodic energy, which is associated from acoustic signals such as clearly defined formants of the kind we see in vowels and other sonorants [42]. In other words, the deviations from periodicity of the signal introduce additional components on inharmonic frequencies. The energy on inharmonic frequencies (sometimes normalized by the total energy) provides a good estimation measure of noise aperiodicity [43].

estimations, regarding to the aforementioned map of irregularities in periodicity, with respect to two different criteria leading to different estimation errors. In our application, we will see later that these two different estimations could be efficiently combine in order to improve the classification result in a (complementary) fusion way, in terms of information interaction [41].

A. Estimation of the Aperiodic Noise Energy in the Temporal Domain

The first step consists in estimating the period T_c of the gait cycle (for each subject) and this can be easily achieved by using the estimation method in the temporal domain described by Cutler and Davis [44]. In this technique, a similarity matrix, comparing all frames of the video sequence, in pairs, is first computed (see Fig. 2). More precisely, let F^k and F^l be two frames of the video of size $H \times W$. The similarity value between F^k and F^l , is given by:

$$S_{F^k, F^l} = \sum_{i=1}^H \sum_{j=1}^W |F_{i,j}^k - F_{i,j}^l| \quad (1)$$

and from this squared symmetric similarity matrix S of size $N_i \times N_i$ (with N_i the number of images in the sequence used in the estimation of T_c), its auto-correlation matrix² $A(d_x, d_y)$ (see Fig. 2) allows us to highlight the peak values that will enable to estimate the gait period T_c :

$$A(d_x, d_y) = \frac{\sum (S_{x,y} - \bar{S})(S_{x+d_x, y+d_y} - \bar{S}_d)}{\sqrt{\sum (S_{x,y} - \bar{S})^2 \sum (S_{x+d_x, y+d_y} - \bar{S}_d)^2}} \quad (2)$$

where the different summations are over all pixel locations (x, y) in the image. \bar{S} and \bar{S}_d are respectively the mean of the similarity matrix and the mean of the shifted similarity matrix. d_x and d_y represents respectively the shift relative to the height and width axis. In Fig. 2.(b), the peaks regularly spaced (in a planar lattice) by T_c pixels (in length or width), spatially show the strong temporal correlations existing between image frame at time k and frame at time $k + T_c$ in the video sequence. In addition, the regularity of these peaks both demonstrates that the video contains a periodic motion with a period equal to T_c , in terms of number of image frames (or $T_c \Delta$, in terms of time, with Δ denoting the time between each frame) and that the video remains stationary over the time (*i.e.*, the period T_c of the gait cycle do not sensitively change during the time study). As the autocorrelation matrix is robust to noise and stationary over the time, the period T_c of the gait cycle is

²The auto-correlation 2D function is itself periodic with the same period as the similarity matrix (or the video sequence) but has the advantage of being much more robust to noise.

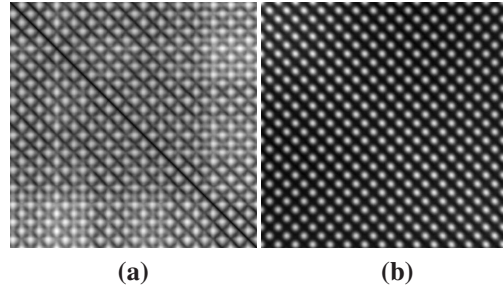


Fig. 2. (a) Images of the similarity matrix S and (b) its auto-correlation function $A(d_x, d_y)$ for the 512 frames of the video and for the S05B patient (B: with a heel under the left foot).

simply estimated by the average distance existing between two peaks. This can be done by any procedure returning the local maxima (peaks) of an input signal (e.g., a local peak is a data sample that is larger than its two neighboring samples). From the previously estimated gait period T_c , the following step consists of the computation of the noiseless periodic pattern for each depth signal, related to each pixel of the subject silhouette.

1. This step(see step 1. of algorithm 1) is based, in fact, on the simple averaging, in the time domain, of multiple and (non-overlapping) consecutive segments of the depth signal of length T_c . In this context, it is well known that appropriate averaging can increase the Signal to Noise Ratio (SNR), especially for Gaussian noise processes. In the later case, averaging N samples will reduce the mean root mean square (rms) current noise by a factor of \sqrt{N} , or the mean noise power by a factor of $1/N$ [45]. Thus, to this end, we subdivide the depth signal s_{depth} (of length T) into successive signals of length T_c and estimate an average pattern s_{patt} which is therefore less noisy.

2. The final step(see step 2. of algorithm 1) consists in computing, for each pixel of the subject silhouette, the difference between the original (noised) depth signal and its related noiseless periodic pattern (modulo T_c). This difference signal represents the (aperiodic) noise signal $n(t)$ of each depth signal, which is then squared integrated over $T \gg T_c$ (T is the length of the depth signal), in order to compute the (temporal) energy of this aperiodic noise in the temporal domain. To this end, we use the classical numerical integration formula [46]:

$$\underbrace{n_{\text{depth}}^s}_{\text{Aperiodic Noise Energy}} = \sum_{t=0}^T \underbrace{\left| s_{\text{depth}}(t) - s_{\text{patt}}(t \bmod T_c) \right|^2}_{n(t)} \quad (3)$$

**Estimation of the aperiodic noise energy
in the temporal domain**

s_{depth} Depth signal for each pixel in the subject silhouette (size: $depth$) (Input)
 T_c Depth signal period (Input)
 n_{depth}^s Aperiodic noise energy of the depth signal (Output)
 s_{patt} Noiseless periodic pattern (size: T_c)
 c_{patt} Vector containing the number of times that a point of the periodic pattern occurred in the depth signal (size: T_c)

Initialization:

```

▷ for each  $i \in [0, \dots, T_c[$  do
  |  $s_{patt}[i] \leftarrow 0.0$  and  $c_{patt}[i] \leftarrow 0$ 
end

```

1. Compute the noiseless periodic pattern

```

▷ for each  $i \in [0, \dots, depth[$  do
  |  $s_{patt}[i \bmod T_c] \leftarrow s_{patt}[i \bmod T_c] + s_{depth}[i]$ 
  |  $c_{patt}[i \bmod T_c] \leftarrow c_{patt}[i \bmod T_c] + 1$ 
end

```

```

▷ for each  $i \in [0, \dots, T_c[$  do
  |  $s_{patt}[i] \leftarrow s_{patt}[i] / c_{patt}[i]$ 
end

```

2. Compute the aperiodic noise energy

```

 $n_{depth}^s \leftarrow 0$ 
▷ for each  $i \in [0, \dots, depth[$  do
  |  $n_{depth}^s += (s_{depth}[i] - s_{patt}[i \bmod T_c])^2$ 
end

```

Algorithm 1: Estimation of the aperiodic noise energy, in the temporal domain, for each pixel s in the subject silhouette

where s_{patt} is the noiseless periodic pattern (of length T_c) estimated in the previous (first) step. The above-mentioned two steps of the estimation of the aperiodic noise energy (in the temporal domain), for each pixel of the subject silhouette, are shown, in pseudo code form, in Algorithm 1.

Each estimated noise energy value, related to each pixel of the subject silhouette, represents thus, in our application, the amount of gait irregularities, in terms of periodicity, of each depth signal, or equivalently (since the treadmill and the depth camera remains fixed during the gait), of each body part of the subject during his gait cycle. This map is also capable

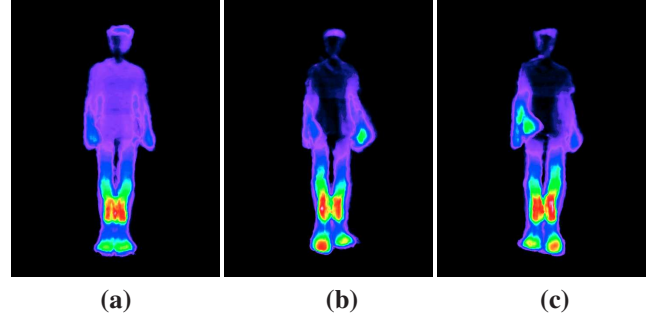


Fig. 3. Periodicity irregularity maps for S05 subject (map obtained in the temporal domain). From left to right: (a) Without a heel (b) Heel under left foot (c) Heel under right foot.

of showing the areas of strongest gait irregularities. In our application, this map is visualized in pseudo-color using the thermal scale (from dark blue-cold to red for white spot) in order to make some details more visible (see Fig. 3 and 4).

B. Estimation of the Aperiodic Noise Energy in the Frequency Domain

In order to estimate, in the frequency domain, the noiseless periodic pattern of the depth signal (related to each pixel) we rely on the Parseval's theorem which specifies that the signal energy is preserved by the Fourier transform across the time and frequency domains [46]. So, let $n(t)$ be the aperiodic noise signal in the temporal domain and $X(\nu)$, its discrete Fourier transform (DFT). Parseval's equality allows us to write that the aperiodic noise energy expressed, in the time and frequency domain, is equal, *i.e.*; $n_{depth}^s = \sum_{t=0}^T |n(t)|^2 = (1/T) \cdot \sum_{\nu=0}^T |X(\nu)|^2 = n_{depth}^f$, where $|X(\nu)|^2$ is called the power spectrum or the power spectral density (PSD) of the aperiodic noise signal. Moreover, in the frequency domain, the energy of the aperiodic noise signal (n_{depth}^f) is simply the summation of the difference between the PSD of the (noisy) depth signal $s_{depth(t)}$ and $|X_{patt}(\nu)|^2$, the PSD of the noiseless periodic pattern $s_{patt}(t)$ according to the following formula:

$$\underbrace{n_{depth}^f}_{\text{Aperiodic Noise Energy}} = \sum_{\nu=0}^T \left| |X(\nu)|^2 - |X_{patt}(\nu)|^2 \right| \quad (4)$$

Thus, in order to efficiently estimate $|X_{patt}(\nu)|^2$, we rely on the estimation of the mean periodogram introduced by Welch [47]. This improved estimator³ of the power spectrum density (PSD) consists of dividing the temporal signal of depth into

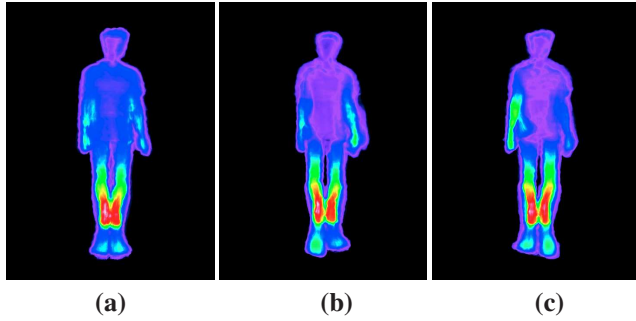


Fig. 4. Periodicity irregularity maps for S05 subject (map obtained in the frequency domain). From left to right: (a) Without a heel (b) Heel under left foot (c) Heel under right foot.

(possibly) overlapping segments x_b . Each segment is weighted by a smooth (e.g., Hamming or Hanning) window⁴ and is then processed by a DFT in order to obtain the modified periodogram $|X_b(\nu)|^2$. The averaging of these modified periodograms allows us to estimate the Welch's PSD estimate [47] $|X_W(\nu)|^2$. This averaging (of modified periodograms) tends to decrease the variance of the PSD estimate relative to a single periodogram estimate of the entire data record. By this fact, the variance is reduced by a factor of L over the periodogram, L being the number of blocks used in the averaging. In our application, we use an overlapping of 50% for segments of length T_s weighted by an Hanning window (and for a length of an entire data record $T = 512$). In addition, we found that the classification rate is also improving as the length T_s decreases until the value $T_s = 16$ (see Fig. 5). This gives us a total number of $L = 63$ block segments (used in the averaging) leading to a PSD estimate with a variance reduced by $L = 63$ compared to single periodogram estimation.

The integration of the difference (see Eq. (4)) between the Welch's mean periodogram $|X_W(\nu)|^2$ (of length $T_s = 16$) and the periodogram of each $|X_b(\nu)|^2$ allows us to give an estimation, in the frequency domain, of the irregularities in terms of periodicity or the degree of aperiodicity (the so-called aperiodic noise energy) existing in each depth signal.

C. Automatic Classification of the Subjects

The two maps of aperiodic noise energy, estimated in the frequency and temporal domain, contain the same information

³In the sense that this estimator is able to give an estimation which is very robust to noise and thus a quasi-noiseless estimation.

⁴The windowing suppress the discontinuity, and the resulting spurious high frequencies in the frequency analysis, by "tapering" the recorded signal smoothly to zero at the start and end of the recording period.

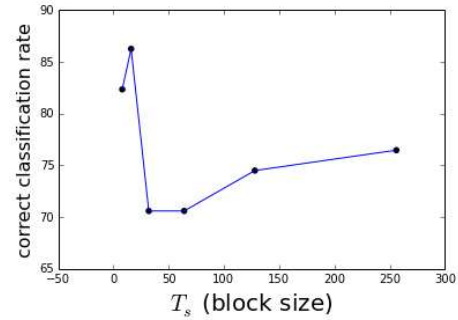


Fig. 5. Curve representing the correct classification rate as a function of T_s , the block size.

but are degraded with different estimation errors. More precisely, these estimation errors are mainly due, in the temporal domain, to the estimation of the period T_c (of the gait cycle) from the autocorrelation of the similarity matrix and mainly due, in the frequency domain, both to the choice of the window (or apodization) function which slightly modified the spectrum (causing leakage⁵) and the window size $T_s < T$ which reduced the frequency resolution of the spectrum and consequently, bias the amplitudes and shape of the spectrum.

At this stage the estimated maps are highly discriminant for a direct visual classification by the clinician (which can also easily localize the problematic or aperiodic noise parts of the patient's body), or even for a non-specialist (Figures 3 and 4 show that for a subject without a heel, the irregularities of periodicity are identically distributed on either side of the axis of symmetry of the silhouette while for subjects with heel, the irregularities of periodicity are larger for the member with heel). Nevertheless, in order to propose a fully automated gait analysis system, we have also developed a classification scheme based on the extraction of the following features obtained from each obtained map. We classified the maps into two classes, namely healthy individuals and those representing individuals with orthopedic problems (with the left or right foot) and three classes (subject without heel under foot, with heel under left foot, with heel under the right foot).

1) *Feature Extraction Step:* These features are divided into two major categories. The first group estimates the degree of difference of the aperiodicity noise energy level (or degree of irregularity, in terms of periodicity) between the left and the right leg for each individual and for a height at a given vertical position (see algorithm 4). In fact, it is expected that there is a larger concentration of aperiodic noise energy on the

⁵Different types of windows will have different leakage-properties.

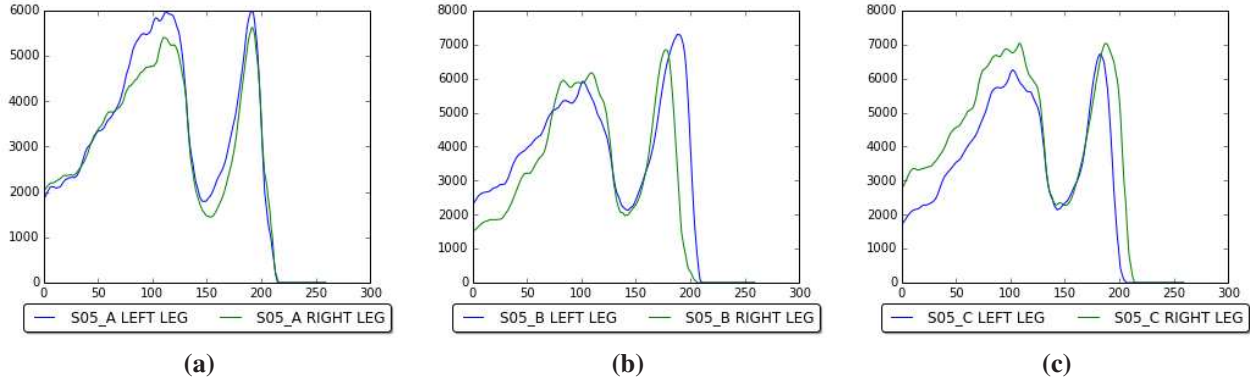


Fig. 6. Curves obtained by the estimation of the aperiodic noise energy achieved in the temporal domain (as a function of the pixel number) representing the two vectors of the horizontal summations of the aperiodic noise energy for different values of height (from top to bottom) of the left and the right leg, for *S05* subject: (a) Without heel (b) Heel under left foot (c) Heel under right foot.

side with the (simulated orthopedic) problem comparatively to the other side. In order to exploit this discriminant property, the horizontal summations of the aperiodic energy values, for different values of height, from top to bottom of the left and the right leg, are stored in two different vectors for each individual.

This interesting feature vector is shown by the curves that display the aforementioned vectors for a subject with or without simulated length leg discrepancy (see Fig. 6). The figure shows that for subjects without heel under the foot, the curves are almost identical, but the difference is very remarkable for subjects with heel. This suggests that this difference of aperiodic noise energy (for the left and the right leg) provides an interesting and a discriminant feature vector for classification.

The second group of features is related to the deformation or the shape of the silhouette generated by the walking action in the video sequence (and thus is not directly related to the aforementioned concept of aperiodic noise energy). Indeed, the presence of problems or pain in lower limbs (or in the body in general) may disrupt the body's alignment and posture. More precisely, for a healthy gait, the right arm swings in the same direction as the left leg, and conversely with a certain symmetry, in terms of arm and leg swings and approximating, in fact, a (regular and periodical) symmetrical pendular movement.

In order to now model the potential disruption related to a possible asymmetry between the left arm and right leg and vice-versa, we consider the following operations:

- 1) From the silhouette (given by the set of non-zero values of the) aperiodic noise energy map I (see Fig. 7.(a)), we estimate the silhouette asymmetry $AS(I)$, by a simple logical "exclusive or" operation between the left and

right part (and conversely) of the binary silhouette (around the preliminary estimated longitudinal axis x_{sym}) (see Algorithm 2 and Fig. 7.(c)).

- 2) We divide the silhouette (see Fig. 7.(a)) into two parts (the lower limbs [between $\frac{3}{5}H$ and H with H the image height] and the upper part of the body above the lower limbs [between 0 and $\frac{3}{5}H$ with H the image height]). Each part is then further divided into two sub-parts (the left and the right parts of the longitudinal axis) for a total of four parts (P_1, P_2, P_3 and P_4) (see Fig. 7.(b)). On these four parts, we compute $SURFA_1$ and $SURFA_2$, the number of pixels (or surface areas) located, above the lower limbs, respectively, to the left and to the right of x_{sym} on $AS(I)$. We also compute $SURFA_3$ and $SURFA_4$, the number of pixels located, for the lower limbs, respectively, to the left and to the right of x_{sym} on $AS(I)$ (see Fig. 7.(c)). Concretely, the parameters $SURFA_i$ represent (in terms of number of pixels), the asymmetry degree (or magnitude) of the facial silhouette between the right and left parts of the body during consecutive gait cycles.
- 3) We now compute SIL_1 and SIL_2 , the two parameters estimated, in the following way:

$$SIL_1 = 2 \times (SURFA_1 + SURFA_4) \quad (5)$$

$$SIL_2 = 2 \times (SURFA_2 + SURFA_3) \quad (6)$$

Concretely speaking, the parameters $SIL_{1,2}$ represent, the degree or magnitude of asymmetry swing between the left arm and the right leg and vice-versa during gait.

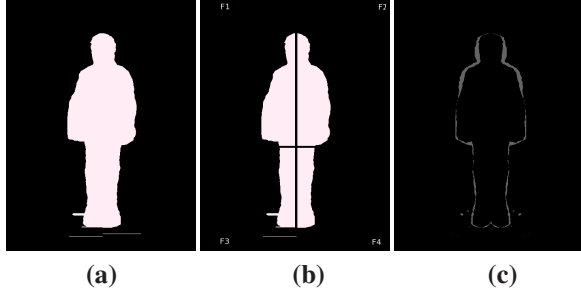


Fig. 7. Estimation of $AS(I)$, the (asymmetry) deformation of the silhouette of the aperiodic energy map I (subject $S17_A$). From left to right. (a) The silhouette (defined by the set of non-zero values of aperiodic noise energy I) on either side of the preliminary estimated longitudinal axis x_{sym} (see Algorithm 2). (b) The silhouette divided into four parts: P_1 , P_2 , P_3 and P_4 . (c) Estimation of the silhouette asymmetry $AS(I)$, between the left and right part of the silhouette (given by a simple logical “exclusive or” operation between the left and right part of the binary silhouette and then symmetrized around the longitudinal axis x_{sym}).

4) In addition, we estimate the following two features:

$$Feat_2 = \frac{(SIL_1 - SIL_2)}{SIL_1} \text{ if } (SIL_1 > SIL_2) \quad (7)$$

$$\text{or: } Feat_2 = \frac{(SIL_2 - SIL_1)}{SIL_2} \text{ if } (SIL_2 > SIL_1) \quad (8)$$

Finally, $Feat_2$ quantify the maximum amplitude, in terms of number of pixels, of irregularity, or asymmetry existing in the left arm swing and right leg movement (or conversely) during consecutive gait cycles (or the asymmetric arm and leg swings motion). We multiply the feature value $Feat_2$ by 1000 in order to equal weight its importance relatively to the first feature vector related to the asymmetry of the aperiodic noise energy (see algorithm 4).

In all, the dimensionality size of the feature vector, used as input for classification, for the temporal and frequency domain separately, is 261 (*i.e.*, 260 features for the first group of feature, corresponding to the curve (of length 260) of difference between the left and the right’s periodicity irregularity of the lower limb (see Fig. 6) plus 1 feature, the 261st, belonging to the second group (see Section III-C.1, and corresponding to the deformation of the silhouette (see Eq. (7) or Eq. (8)). When the feature vector, in temporal and in frequency domain, is placed side by side; the vector size is 522. After using PCA, the dimensionality size is reduced to 51.

IV. EXPERIMENTAL RESULTS

In our application, the depth of the video cube, to be processed is $T = 512$, which corresponds to a gait video

sequence of about 17 seconds (for a Kinect capturing 30 frames per second).

First, concerning the estimation of the aperiodic noise energy in the temporal domain, we can notice on the similarity matrix (see Fig. 2) a dark line on the diagonal, that emphasizes the fact that each frame of the video is similar to itself, and also a periodic pattern identical in the vertical and horizontal direction, showing that the human gait exhibits a clear periodic motion [44]. The auto-correlation function of the similarity matrix (see Fig. 2) is itself periodic with the same period T_c as the similarity matrix (or the video sequence) but has the important advantage of being much more robust to noise since each value of the auto-correlation function results from the integration over all values of the similarity matrix. The period T_c of the gait cycle is, of course, slightly different for each subject, but remains about 36 ± 4 .⁶

Consequently, the estimation of the noiseless periodic pattern of each depth signal (related to each pixel of the subject silhouette and required in the estimation of the aperiodic noise energy map in the temporal domain, see Section III-A), is based on the averaging of $T/T_c \approx 14.22$ depth signals which thus leads to a periodic pattern altered by a mean noise power approximately reduced by a factor around 15 (or a periodic pattern with less than $100/14.22 \approx 7\%$ of aperiodic (irregularity) energy).

Second, concerning the estimation of the aperiodic noise energy in the frequency domain, we recall that we use an overlapping of 50% for segments of length $T_s = 16$, weighted by an Hanning window, for a total of $L = 63$ block segments, used in the averaging, and leading to a PSD estimate with a variance reduced by $L = 63$ compared to single periodogram estimation.

The examples shown in Fig. 6, 8 and 9 confirm that the difference of aperiodicity curves, along with the parameter quantifying the asymmetric arm and leg swings motion, provide complementary and relevant features for our classification problem. More precisely, the curve for the right leg and the curve for the left leg tends to coincide for subjects without heel whereas the curve tends to move away from one another for subjects with a heel. In Fig. 8, the curve of the difference of the curves in Fig. 6, tends to touch the x-axis for subjects with heel while for subjects without their heel, the curves are less close to the x-axis. In Fig. 9, the deformation, evidenced

⁶ 36 ± 4 means that 99% of the gait period estimations, obtained on the set of 17 subjects, are, in terms of number of frames, within the confidence interval [32, ..., 40] among the subjects (*i.e.*, the shortest gait period is 32 frames and the longest is 40 frames). In terms of seconds, by remembering that the kinect outputs 30 frames per second, it defines the following confidence interval: $[\approx 1.06 \text{ seconds}, \dots, \approx 1.34 \text{ seconds}]$.

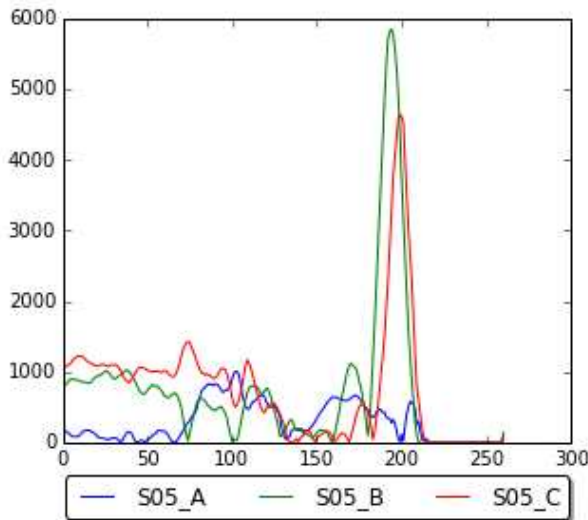


Fig. 8. Curves obtained by the estimation of the aperiodic noise energy achieved in the temporal domain (as a function of the pixel number) representing the absolute value of the difference of the two vectors of the horizontal summations (i.e., summation over the columns) of the aperiodic noise energy for different values (from top to bottom) of height, of the left and right leg, of the subject $S05$, for the three considered cases, namely; $S05_A$: subject without the heel; $S05_B$: subject with the heel under the left foot; $S05_C$: subject $S05$ with the heel under the right foot.

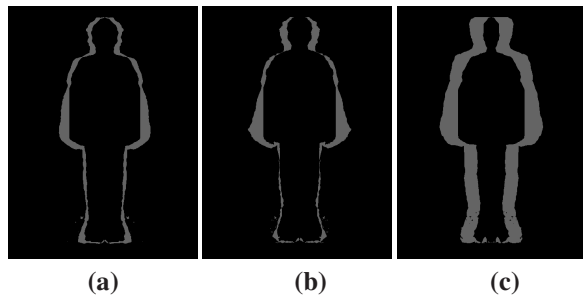


Fig. 9. Silhouette deformation maps for the $S06$ subject. From left to right; (a) without heel (b) heel under the left foot (c) heel under the right foot.

by the white pixels, is larger for subjects with heel and smaller for subjects without a heel.

The automatic classification of the subjects walking on the treadmill is studied through Gaussian Naive Bayes (GNB), k-Nearest Neighbors (KNN), Logistic Regression (LR), Support Vector Machine (SVM) and Stochastic Gradient Descent (SGDC) classifiers from the Python's scikit-learn library [48]. The 51 examples are randomly ordered and we use the cross-validation (leave one cross-validation) technique because we have relatively small data set (51 examples). The kernel for

SVM with the best rates for two classes is the radial basis function (rbf kernel). For the ternary (i.e., three classes) classification problem, it is the cubic polynomial kernel that gave the best rates.

The classification results into two or three classes are respectively shown in Table I and Table II both for individual state-of-the-art classification model used in the literature and exploiting the features extracted from either our aperiodic energy map obtained in the temporal domain or in the frequency domain and also for a simple multiple classifier system whose decisions are then combined through the combination of the estimates obtained from each individual base classifier with the simple majority voting decision rule. The experiments have been tried and tested with or without pre-processing by Principal Component Analysis (PCA) and with or without scaling (the PCA and the scaler are from scikit-learn library [48]).

In addition, we show the classification results into two or three classes with a different fusion strategy (between the feature vector extracted from the aperiodic energy map estimated in the frequency and temporal domains) and consisting simply in concatenating the two feature vectors into a single feature vector (see Table III).

We can also notice that the performance of classifiers to the aperiodic energy maps obtained in the temporal or frequency domains are also somewhat different which in fact makes a multiple classifier based strategy a reliable classification algorithm for our two class classification problem. It also shows that these two maps are complementary and can be effectively combined.

Finally, the results show that the two-class classification problem ("normal" or "abnormal" gait) gives excellent results, especially with a multiple classifier system and the first fusion strategy (see Table I). On the other hand, the three-class classification problem is more complex and the results are disappointing (whatever the fusion strategy used). This can be explained by the fact that the physical behavior of each individual, in terms of response to the presence of a heel (placed below the right or left foot) may be very different across individuals (some of them answer to the problem by a greater oscillation of one arm (or the two arms), or a greater (or smaller or different) stride length, etc.

V. CONCLUSION

In this work, we have presented a new gait analysis system based on features extracted from the estimation of an aperiodic noise energy map which aims at showing the areas of strong irregularities of the gait, in terms of periodicity, of each subject

International Journal of Emerging Technology and Advanced Engineering
Website: www.ijetae.com (ISSN 2250-2459, Volume 9, Issue 5, May 2019)

TABLE I

CLASSIFICATION RATES OF 51 PERIODICITY IRREGULARITY MAPS OF 17 SUBJECTS INTO TWO CLASSES (NORMAL OR NOT) (LOOCV: LEAVE ONE OUT CROSS-VALIDATION, LR: LOGISTIC REGRESSION, SVM: SUPPORT VECTOR MACHINE, KNN: K-NEAREST NEIGHBORS, GNB: GAUSSIAN NAIVE BAYES, SGDC: STOCHASTIC GRADIENT DESCENT CLASSIFIER, PCA: PRINCIPAL COMPONENT ANALYSIS)

TEMPORAL DOMAIN					
LOOCV with:	Accuracy:	Precision:	Sensitivity (Recall):	Specificity:	F₁ Score:
KNN with scaling	90.20%	96.77%	88.23%	94.12%	0.9231
SVM (kernel:RBF) with scaling	88.23%	91.18%	91.18%	82.35%	0.9118
GNB with PCA preprocessing	84.31%	84.21%	94.12%	64.70%	0.8889
LR with scaling	82.35%	87.88%	85.29%	76.47%	0.8657
FREQUENCY DOMAIN					
LOOCV with:	Accuracy:	Precision:	Sensitivity (Recall):	Specificity:	F₁ Score:
SVM(kernel:polynomial) with PCA preprocessing	86.27%	90.91%	88.23%	82.35%	0.8955
SVM (kernel:RBF) with scaling	84.31%	80.95%	100.0%	52.94%	0.8947
GNB with PCA preprocessing	82.35%	87.88%	85.29%	76.47%	0.8657
MAJORITY VOTING					
LOOCV with:	Accuracy:	Precision:	Sensitivity (Recall):	Specificity:	F₁ Score:
KNN (spatial), SVM(kernel:RBF) (spatial), SVM(kernel:RBF) (spectral) with scaling	94.12%	94.29%	97.06%	88.23%	0.9565
SVM (kernel:linear)(spatial), KNN(spectral), LR(spectral) with scaling	90.20%	93.94%	91.18%	88.23%	0.9254
KNN (spatial), KNN(spectral), GNB (spatial), GNB(spectral), SVM(kernel:polynomial)(spectral) with PCA preprocessing	88.23%	93.75%	88.23%	88.23%	0.9091

TABLE II

CLASSIFICATION RATES OF 51 PERIODICITY IRREGULARITY MAPS OF 17 SUBJECTS INTO THREE CLASSES (A: WITHOUT HEEL UNDER FOOT, B: WITH HEEL UNDER LEFT FOOT, C: WITH HEEL UNDER RIGHT FOOT) WITH THE SAME CLASSIFIERS AND DATA PROCESSING LIKE ABOVE CLASSIFICATION. LINSVM MENTIONED HERE IS A SVM WITH LINEAR KERNEL BUT IMPLEMENTED IN A DIFFERENT WAY THAN THE OTHER SVM (LINEAR).

TEMPORAL DOMAIN					
LOOCV with:	Accuracy:	Precision:	Sensitivity (Recall):	Specificity:	F₁ Score:
SVM (linSVM) with scaling	68.62%	69%	68.67%	68.62%	0.6867
LR with PCA preprocessing	64.70%	65%	64.67%	64.70%	0.64
SVM (kernel:polynomial) without preprocessing	60.78%	61%	60.67%	60.78%	0.6033
FREQUENCY DOMAIN					
LOOCV with:	Accuracy:	Precision:	Sensitivity (Recall):	Specificity:	F₁ Score:
SVM(kernel:linear) with PCA preprocessing	66.66%	66.33%	66.66%	66.66%	0.6633
LR with PCA preprocessing	64.70%	66.67%	64.67%	64.70%	0.64
SGDC with PCA preprocessing	60.78%	61%	61.33%	60.78%	0.58

TABLE III

CLASSIFICATION RATES FROM FEATURES EXTRACTED FROM THE PERIODICITY IRREGULARITY MAPS IN FREQUENCY AND TEMPORAL DOMAIN AND PLACED SIDE BY SIDE (51 EXAMPLES FOR 17 SUBJECTS).
LOOCV: LEAVE ONE OUT CROSS-VALIDATION, LR: LOGISTIC REGRESSION, SVM: SUPPORT VECTOR MACHINE, KNN: K-NEAREST NEIGHBORS, GNB: GAUSSIAN NAIVE BAYES AND SGDC: STOCHASTIC GRADIENT DESCENT CLASSIFIER, PCA: PRINCIPAL COMPONENT ANALYSIS; LINSVM MENTIONED HERE IS A SVM WITH LINEAR KERNEL BUT BUT IMPLEMENTED IN A DIFFERENT WAY THAN THE OTHER SVM (KERNEL: LINEAR).

TWO CLASSES					
LOOCV with:	Accuracy:	Precision:	Sensitivity (Recall):	Specificity:	F₁ Score:
KNN with or without preprocessing	88.23%	93.75%	88.23%	88.23%	0.9091
GNB with PCA processing	88.23%	88.89%	94.12%	76.47%	0.9143
SVM (kernel:linear) with PCA processing	84.31%	90.63%	85.29%	82.35%	0.8788
LR with scaling	84.31%	93.33%	82.35%	88.23%	0.875

THREE CLASSES					
LOOCV with:	Accuracy:	Precision:	Sensitivity (Recall):	Specificity:	F₁ Score:
LR with PCA preprocessing	68.62%	69.33%	68.66%	68.62%	0.68
KNN with scaling	66.66%	65.33%	66.66%	66.66%	0.6433
SVM(linSVM) with scaling	66.66%	66%	66.66%	66.66%	0.6566
SVM (kernel:linear) with scaling	64.70%	64.33%	64.66%	64.70%	0.6466

walking on a treadmill, and also allows to quantify the degree of asymmetrical (opposite arm and leg) movement patterns. This 2D spatial map is estimated in two complementary ways, namely in the temporal and in the frequency domains in order to get an estimation of the useful information with two different noises and to subsequently provide complementary decisions from different individual classifier which will then be combined. This map also allows for the clinician to visually and quickly localize and quantify the gait abnormalities and for the rehabilitation of patients, to the evolution of these abnormalities over the time. With further analysis across other population including real patients, we also hope this system could be useful or a good indicator to quickly detect a possible disease, or for a rapid but reliable diagnosis, prior to a more thorough examination by a specialist doctor. The system proposed in this paper is also inexpensive, marker-less, non-invasive, easy to set up and requiring a small room. These characteristics qualify it for the daily activities in a clinic. This system also makes an automatic classification of healthy patients and those who are unhealthy with good classification rates.

REFERENCES

- [1] R. Klette and G. Tee, "Understanding human motion: A historic review," *3d Imaging for Safety and Security*, vol. 1, pp. 22–40, 2007.
- [2] J. Rose and J. G. Gamble, *Human walking*. Lippincott Williams & Wilkins Philadelphia, 2006.
- [3] A. Jain, R. Bolle, and S. Pankanti, *Biometrics: personal identification in networked society*. Springer Science & Business Media, 2006, vol. 479.
- [4] D. Cunado, M. S. Nixon, and J. N. Carter, "Automatic extraction and description of human gait models for recognition purposes," *Computer Vision and Image Understanding*, vol. 90, no. 1, pp. 1–41, 2003.
- [5] R. Zhang, C. Vogler, and D. Metaxas, "Human gait recognition," in *Conference on Computer Vision and Pattern Recognition Workshop, 2004. CVPRW'04*. IEEE, 2004, pp. 18–18.
- [6] D. Gafurov, K. Helkala, and T. Söndrol, "Biometric gait authentication using accelerometer sensor," *Journal of computers*, vol. 1, no. 7, pp. 51–59, 2006.
- [7] T. T. Verlekar, L. D. Soares, and P. L. Correia, "Gait recognition in the wild using shadow silhouettes," *Image and Vision Computing*, vol. 76, pp. 1–13, 2018.
- [8] Y. Iwashita and A. Stoica, "Gait recognition using shadow analysis," in *Bio-inspired Learning and Intelligent Systems for Security, 2009. BLISS'09. Symposium on*. IEEE, 2009, pp. 26–31.
- [9] Y. Dupuis, X. Savatier, and P. Vasseur, "Feature subset selection applied to model-free gait recognition," *Image and vision computing*, vol. 31, no. 8, pp. 580–591, 2013.
- [10] C. Strohrmann, H. Harms, C. Kappeler-Setz, and G. Troster, "Monitoring kinematic changes with fatigue in running using body-worn sensors," *IEEE Transactions on Information Technology in Biomedicine*, vol. 16, no. 5, pp. 983–990, 2012.
- [11] C. Bauckhage, J. K. Tsotsos, and F. E. Bunn, "Automatic detection of abnormal gait," *Image and Vision Computing*, vol. 27, no. 1-2, pp. 108–115, 2009.
- [12] L. Palmerini, L. Rocchi, S. Mellone, F. Valzania, and L. Chiari, "Feature selection for accelerometer-based posture analysis in parkinson's disease," *IEEE Transactions on Information Technology in Biomedicine*, vol. 15, no. 3, pp. 481–490, 2011.
- [13] D. T. Lai, P. Levinger, R. K. Begg, W. L. Gilleard, and M. Palaniswami, "Automatic recognition of gait patterns exhibiting patellofemoral pain syndrome using a support vector machine approach," *IEEE Transactions on Information Technology in Biomedicine*, vol. 13, no. 5, pp. 810–817, 2009.

- [14] J. Perry and J. M. Burnfield, *Gait analysis: normal and pathological function*. Slack Incorporated, 2010.
- [15] M. Bächlin, M. Plotnik, D. Roggen, I. Maidan, J. M. Hausdorff, N. Giladi, and G. Tröster, "Wearable assistant for parkinson's disease patients with the freezing of gait symptom," *IEEE Transactions on Information Technology in Biomedicine*, vol. 14, no. 2, pp. 436–446, 2010.
- [16] M. Ermes, J. Parkka, J. Mantyjarvi, and I. Korhonen, "Detection of daily activities and sports with wearable sensors in controlled and uncontrolled conditions," *IEEE Transactions on Information Technology in Biomedicine*, vol. 12, no. 1, pp. 20–26, 2008.
- [17] L. Mündermann, S. Corazza, and T. P. Andriacchi, "Markerless motion capture for biomechanical applications," in *Human Motion*. Springer, 2008, pp. 377–398.
- [18] X. Ma, H. Wang, B. Xue, M. Zhou, B. Ji, and Y. Li, "Depth-based human fall detection via shape features and improved extreme learning machine," *IEEE Journal of Biomedical and Health Informatics*, vol. 18, no. 6, pp. 1915–1922, 2014.
- [19] M. W. Whittle, "Clinical gait analysis: A review," *Human Movement Science*, vol. 15, no. 3, pp. 369–387, 1996.
- [20] A. M. Howell, T. Kobayashi, H. A. Hayes, K. B. Foreman, and S. J. Bamberg, "Kinetic gait analysis using a low-cost insole," *IEEE Transactions on Biomedical Engineering*, vol. 60, no. 12, pp. 3284–3290, 2013.
- [21] "Motion capture systems from vicon." [Online]. Available: <http://www.vicon.com/>
- [22] P. Lopez-Meyer, G. D. Fulk, and E. S. Sazonov, "Automatic detection of temporal gait parameters in poststroke individuals," *IEEE Transactions on Information Technology in Biomedicine*, vol. 15, no. 4, pp. 594–601, 2011.
- [23] S. J. M. Bamberg, A. Y. Benbasat, D. M. Scarborough, D. E. Krebs, and J. A. Paradiso, "Gait analysis using a shoe-integrated wireless sensor system," *IEEE Transactions on Information Technology in Biomedicine*, vol. 12, no. 4, pp. 413–423, 2008.
- [24] R. Moe-Nilssen, "A new method for evaluating motor control in gait under real-life environmental conditions. part 1: The instrument," *Clinical Biomechanics*, vol. 13, no. 4, pp. 320–327, 1998.
- [25] R. Takeda, S. Tadano, M. Todoh, M. Morikawa, M. Nakayasu, and S. Yoshinari, "Gait analysis using gravitational acceleration measured by wearable sensors," *Journal of biomechanics*, vol. 42, no. 3, pp. 223–233, 2009.
- [26] D. M. Karantonis, M. R. Narayanan, M. Mathie, N. H. Lovell, and B. G. Celler, "Implementation of a real-time human movement classifier using a triaxial accelerometer for ambulatory monitoring," *IEEE Transactions on Information Technology in Biomedicine*, vol. 10, no. 1, pp. 156–167, 2006.
- [27] M. Landau, B. Choo, and P. Beling, "Simulating kinect infrared and depth images," *IEEE Transactions on cybernetics*, 2015.
- [28] E. E. Stone and M. Skubic, "Fall detection in homes of older adults using the microsoft kinect," *IEEE Journal of Biomedical and Health Informatics*, vol. 19, no. 1, pp. 290–301, 2015.
- [29] E. Stone and M. Skubic, "Evaluation of an inexpensive depth camera for in-home gait assessment," *Journal of Ambient Intelligence and Smart Environments*, vol. 3, no. 4, pp. 349–361, 2011.
- [30] Z. Zhang, "Microsoft kinect sensor and its effect," *IEEE Multimedia*, vol. 19, no. 2, pp. 4–10, 2012.
- [31] S. Motiian, P. Pergami, K. Guffey, C. A. Mancinelli, and G. Doretto, "Automated extraction and validation of children's gait parameters with the kinect," *BioMedical Engineering OnLine*, vol. 14, no. 11, 2015.
- [32] M. Gabel, R. Gilad-Bachrach, E. Renshaw, and A. Schuster, "Full body gait analysis with kinect," in *2012 Annual International Conference of the IEEE Engineering in Medicine and Biology Society*. IEEE, 2012, pp. 1964–1967.
- [33] M. Milovanovic, M. Minovic, and D. Starcevic, "Walking in colors: human gait recognition using kinect and cbr," *IEEE MultiMedia*, vol. 20, no. 4, pp. 28–36, 2013.
- [34] T.-L. Le, M.-Q. Nguyen *et al.*, "Human posture recognition using human skeleton provided by kinect," in *Computing, Management and Telecommunications (ComManTel), 2013 International Conference on*. IEEE, 2013, pp. 340–345.
- [35] Š. Obdržálek, G. Kurillo, F. Ofli, R. Bajcsy, E. Seto, H. Jimison, and M. Pavel, "Accuracy and robustness of kinect pose estimation in the context of coaching of elderly population," in *2012 Annual International Conference of the IEEE Engineering in Medicine and Biology Society*. IEEE, 2012, pp. 1188–1193.
- [36] J. Han, L. Shao, D. Xu, and J. Shotton, "Enhanced computer vision with microsoft kinect sensor: A review," *IEEE Transactions on cybernetics*, vol. 43, no. 5, pp. 1318–1334, 2013.
- [37] C. Rougier, E. Auvinet, J. Meunier, M. Mignotte, and J. A. de Guise, "Depth energy image for gait symmetry quantification," in *Engineering in Medicine and Biology Society, EMBC, 2011 Annual International Conference of the IEEE*. IEEE, 2011, pp. 5136–5139.
- [38] E. Auvinet, F. Multon, and J. Meunier, "Lower limb movement asymmetry measurement with a depth camera," in *Engineering in Medicine and Biology Society (EMBC), 2012 Annual International Conference of the IEEE*, Aug 2012, pp. 6793–6796.
- [39] A. Moevus, M. Mignotte, J. de Guise, and J. Meunier, "Evaluating perceptual maps of asymmetries for gait symmetry quantification and pathology detection," in *36th International Conference of the IEEE Engineering in Medicine and Biology Society, EMBC'2014*, Chicago, Illinois, USA, August 2014, pp. 3317–3320.
- [40] R. Moe-Nilssen and J. L. Helbostad, "Estimation of gait cycle characteristics by trunk accelerometry," *Journal of biomechanics*, vol. 37, no. 1, pp. 121–126, 2004.
- [41] G.-Z. Yang, *Body Sensor Networks*. Secaucus, NJ, USA: Springer-Verlag New York, Inc., 2006.
- [42] P. Backley, *An introduction to element theory*. Edinburgh University Press, 2011.
- [43] H. Kawahara, J. Estill, and O. Fujimura, "Aperiodicity extraction and control using mixed mode excitation and group delay manipulation for a high quality speech analysis, modification and synthesis system straight," in *Conference MAVEBA*, 2001.
- [44] R. Cutler and L. S. Davis, "Robust real-time periodic motion detection, analysis, and applications," *IEEE Transactions on Pattern Analysis and Machine Intelligence*, vol. 22, no. 8, pp. 781–796, 2000.
- [45] N. E. L. U. E. T. Division, *Optical Fiber Characterization*, ser. NBS special publication. U.S. Department of Commerce, National Bureau of Standards, 1982, no. vol. 1 ;vol. 637. [Online]. Available: <https://books.google.ca/books?id=LrV3rgEACAAJ>
- [46] A. Rihaczek, "Signal energy distribution in time and frequency," *IEEE Transactions on Information Theory*, vol. 14, no. 3, pp. 369–374, 1968.
- [47] P. Welch, "The use of fast fourier transform for the estimation of power spectra: A method based on time averaging over short, modified periodograms," *IEEE Trans. Audio Electroacoust.*, vol. AU-15, pp. 70–73, 1967.
- [48] F. Pedregosa, G. Varoquaux, A. Gramfort, V. Michel, B. Thirion, O. Grisel, M. Blondel, P. Prettenhofer, R. Weiss, V. Dubourg, J. Vanderplas, A. Passos, D. Cournapeau, M. Brucher, M. Perrot, and É. Duchesnay, "Scikit-learn: Machine learning in python," *The Journal of Machine Learning Research*, vol. 12, pp. 2825–2830, 2011.

VI. ACKNOWLEDGEMENT

Ethical approbation was obtained from the research ethics board of our university for this project.

APPENDIX: ALGORITHMS

Estimation of the longitudinal axis estimation

I Aperiodic noise map (size: $height \times width$) (Input)
 x_{sym} Longitudinal axis estimation (Output)
 r Size of the search interval
 G_I Gradient magnitude map of I
Vct Vector of floats of size $height$
 x_{sym} Column coord. estimation of the longitudinal axis

Initialization : $G_I \leftarrow$ gradient magnitude map of I

1. Longitudinal Axis Estimation

```

▷ for each  $i \in [0, \dots, height[$  do
  grdMx  $\leftarrow 0$ 
  ▷ for each  $j \in [(width/2) - r, \dots, (width/2) + r[$ 
    do
      ▷ for each  $m \in [0, \dots, width/2[$  do
        grd  $\leftarrow G_I[i][j - m] + G_I[i][j + m]$ 
        if (grd > grdMx) { pos  $\leftarrow j$   grdMx  $\leftarrow$  grd }
      end
    end
  end
  Vct[i]  $\leftarrow$  pos
end
 $x_{sym} \leftarrow$  median value of the vector elements Vct[]

```

Algorithm 2: Estimation of the longitudinal axis estimation

Estimation of depth signal noise in frequency domain using the averaged Welch's periodogram

s_{depth} Depth signal in temp. domain (sz: $depth$) (Input)
 b_dim Block dimension (Input)
 n_{depth}^f Aperiodic noise energy of s_{depth} (Output)
 X_{awp} Averaged Welch's periodogram (sz: b_dim)
 N_{depth} Noise vector in freq. domain (sz: $depth$)
 n_b Number of blocks
 h_w Hanning window (sz: b_dim)
 x_b Sub-block of s_{depth} in temp. domain (sz: b_dim)
 N_t Temporary vector (sz: $depth$)

Initialization : $n_b \leftarrow 0$ $k \leftarrow 0$

```

for each  $i \in [0, \dots, b\_dim[$  do
  |  $h_w[i] \leftarrow 0.54 - 0.46 \cos(2\pi \frac{i}{b\_dim})$    $X_{awp}[i] \leftarrow 0$ 
end

```

1. Averaged Welch's periodogram estimation

```

▷ for each  $j = 0$  to  $(depth - b\_dim)$  with  $j += b\_dim$ 
do

```

```

  |  $n\_b \leftarrow n\_b + 1$ 
  | ▷ for each  $i \in [0, \dots, b\_dim[$  do
  |   |  $x_b[i] \leftarrow s_{depth}[i + j] \times h_w[i]$ 
  |   end
  |    $X_{mdl} \leftarrow |FFT1D(x_b)|$ 
  |   ▷ for each  $i \in [0, \dots, b\_dim[$  do
  |     |  $N_t[k] \leftarrow (X_{mdl}[i])^2$ 
  |     |  $X_{awp}[i] \leftarrow X_{awp}[i] + (X_{mdl}[i])^2$    $k \leftarrow k + 1$ 
  |     end
  |   end
end

```

```

▷ for each  $j = \frac{b\_dim}{2}$  to  $(depth - \frac{b\_dim}{2})$  with  $j += b\_dim$ 
do

```

```

  |  $n\_b \leftarrow n\_b + 1$ 
  | ▷ for each  $i \in [0, \dots, b\_dim[$  do
  |   |  $x_b[i] \leftarrow s_{depth}[i + j] \times h_w[i]$ 
  |   end
  |    $X_{mdl} \leftarrow |FFT1D(x_b)|$ 
  |   ▷ for each  $i \in [0, \dots, b\_dim[$  do
  |     |  $X_{awp}[i] \leftarrow X_{awp}[i] + (X_{mdl}[i])^2$ 
  |     end
  |   end
end

```

```

▷ for each  $i \in [0, \dots, b\_dim[$  do  $X_{awp}[i] \leftarrow \frac{X_{awp}[i]}{n\_b}$ 

```

2. Depth signal noise estimation in frequency domain

```

▷ for each  $i \in [0, \dots, depth[$  do
 $N_{depth}[i] \leftarrow (N_t[i] - X_{awp}[i \text{ modulo } b\_dim])$ 
 $n_{depth}^f \leftarrow 0$ 
▷ for each  $i \in [0, \dots, depth[$  do  $n_{depth}^f += |N_{depth}[i]|$ 

```

Algorithm 3: Estimation of the depth signal noise in frequency domain using averaged Welch's periodogram with a 50% overlapping between blocks of size b_dim



Didier Ndayikengurukiye received the M.Sc. degree in computer science in 2016 from the University of Montreal, Department of Computer Science and Operations Research (DIRO), Montreal, QC, Canada. He is currently a Ph.D. student at vision laboratory of the university of Montreal (DIRO).



Max Mignotte received the DEA (Postgraduate degree) in Digital Signal, Image and Speech processing from the INPG University, France (Grenoble), in 1993 and the Ph.D. degree in electronics and computer engineering from the University of Bretagne Occidentale (UBO) and the digital signal laboratory (GTS) of the French Naval academy, France, in 1998. He was an INRIA post-doctoral fellow at University of Montreal (DIRO), Canada (Quebec), from 1998 to 1999. He is currently with DIRO at the Computer Vision & Geometric Modeling Lab

as a Professor at the University of Montreal. He is also a member of LIO (Laboratoire de recherche en imagerie et orthopedie, Centre de recherche du CHUM, Hopital Notre-Dame) and researcher at CHUM. His current research interests include statistical methods, Bayesian inference and hierarchical models for high-dimensional inverse problems such as segmentation, parameters estimation, fusion, shape recognition, deconvolution, 3D reconstruction and restoration problems.

Estimation of the features

I	Aperiodic noise energy map (size: $height \times width$) (Input)
x_{sym}	Longitudinal axis estimation (column coordinate) (Input)
C_l, C_r	Vector of the horizontal summation of the aperiodic noise energy for the left (right) area of the longitudinal axis of the lower limbs (size: $height - h$) (Output)
C	Vector for the difference of C_l and C_r ; and the value of the silhouette asymmetry (size: $height - h + 1$) (Output)
h	Row coord. of the beginning of the lower limbs of I ($h = 380$)
$AS(I)$	Silhouette asymmetry map of I
$SURFA_{1,2}$	Number of pixels located to the left and to the right of x_{sym} respectively above the lower limbs (on $SA(I)$)
$SURFA_{3,4}$	Number of pixels located to the left and to the right of x_{sym} respectively for lower limbs part (on $SA(I)$)

1. Computation of vectors C_l , C_r and C

```

k ← 0
▷ for each i ∈ [h, ..., height] do
  m_l ← 0
  ▷ for each j ∈ [0, ..., x_sym] do m_l ← m_l + I[i][j]
  C_l[i - h] ← m_l
  m_r ← 0
  ▷ for each j ∈ [x_sym, ..., width] do m_r ← m_r + I[i][j]
  C_r[i - h] ← m_r
  C[k] ← |m_l - m_r|
  k ← k + 1

```

end

2. Computation of the silhouette asymmetry features

$x_{sym} \leftarrow$ Longitudinal axis estimation [I] (cf. Algorithm 2.)

$AS(I) \leftarrow$ “exclusive or” operation around the column coordinate x_{sym} of the binary silhouette I

$SURFA_{1,2,3,4} \leftarrow$ number of pixels located respectively above (right and left) and on the lower limbs

$SIL_1 \leftarrow 2 (SURFA_1 + SURFA_4)$

$SIL_2 \leftarrow 2 (SURFA_2 + SURFA_3)$

if ($SIL_1 > SIL_2$) $C[k] \leftarrow 1000 (SIL_1 - SIL_2) / SIL_1$

else $C[k] \leftarrow 1000 (SIL_2 - SIL_1) / SIL_2$

Algorithm 4: Estimation of the features